Journal Pre-proof

A coupled isogeometric/multi-sphere discrete element approach for the contact interaction between irregular particles and structures

Wei Gao, Y.T. Feng, Chengyong Wang

PII: S0032-5910(23)00754-4
DOI: https://doi.org/10.1016/j.powtec.2023.118971
Reference: PTEC 118971

To appear in: *Powder Technology*

Received date : 11 June 2023
Revised date : 28 August 2023
Accepted date : 7 September 2023

Please cite this article as: W. Gao, Y.T. Feng and C. Wang, A coupled isogeometric/multi-sphere discrete element approach for the contact interaction between irregular particles and structures, *Powder Technology* (2023), doi: https://doi.org/10.1016/j.powtec.2023.118971.

This is a PDF file of an article that has undergone enhancements after acceptance, such as the addition of a cover page and metadata, and formatting for readability, but it is not yet the definitive version of record. This version will undergo additional copyediting, typesetting and review before it is published in its final form, but we are providing this version to give early visibility of the article. Please note that, during the production process, errors may be discovered which could affect the content, and all legal disclaimers that apply to the journal pertain.

© 2023 Elsevier B.V. All rights reserved.

Journal Pre-proof

A coupled isogeometric/multi-sphere discrete element approach for the contact interaction between irregular particles and structures

Wei Gao[a,b,*], Y.T. Feng[c,*], Chengyong Wang[a,b,d]

[a]School of Electromechanical Engineering, Guangdong University of Technology, Guangzhou, China
[b]Guangdong Provincial Key Laboratory of Minimally Invasive Surgical Instruments and Manufacturing Technology, Guangdong University of Technology, Guangzhou, China
[c]Zienkiewicz Centre for Computational Engineering, Swansea University, Swansea, UK
[d]State Key Laboratory for High Performance Tools, Guangdong University of Technology, Guangzhou, China

Abstract

An isogeometric/multi-sphere discrete-element coupling method is presented to model the contact or impact between structures and particles with complex shape. This coupling method takes advantages of the multi-sphere discrete element method for particles to provide the high computational efficiency and excellent robustness of their contact modelling. The advantage of isogeometric analysis (IGA) for continuous solid material, e.g. the exact geometric description, is also taken to achieve a more accurate contact interaction with an excellent time continuity. In the coupling procedure, the CGRID method is used for the global searching. The exact contact situation of the

*Corresponding author. Wei Gao, Tel.: +86 15218869879; Y.T. Feng, Tel.: +44 (0)1792295161

Email addresses: gaowei@gdut.edu.cn; hbweigao@126.com (Wei Gao), y.feng@swansea.ac.uk (Y.T. Feng)

Journal Pre-proof

Journal Pre-proof

discrete element and the IGA element surface is further determined in the local searching by solving non-linear equations numerically. Then, the normal contact force between a sphere and an IGA element is calculated using a penalty based Hertz-Mindlin contact model, and damping and friction forces are also considered. Both the accuracy and validity of the coupling method are examined by comparing the numerical results of an example with one particle impacting on a quarter of a cylinder, with those of the FEM model where the particle is modeled as a rigid body. Two additional examples involving particles impacting onto a corrugated plate and particles of different shapes impacting on a chute, are simulated to further assess the applicability and robustness of the proposed method.

Keywords: Isogeometric analysis, Multi-sphere particle, Coupling, Contact interaction, IGA/DEM

1. Introduction

The discrete element method, originally developed by Cundall and Strack in the 1970s [1, 2], has been widely recognised as an effective approach for modelling granular materials, including their flow and mixing behaviour. Granular materials often consist of particles with complex shapes, which significantly influence their mechanical behaviour [3]. The multi-sphere discrete element method (MS-DEM) [4, 5] is a popular technique that connects (overlapping) spheres to represent non-spherical particles in an approximate fashion. For simulations where the numerical results are sensitive to the accu-

Journal Pre-proof

racy of shape representation, more accurate shape descriptions for particles, such as the surface meshed DEM [6, 7, 8, 9], the level set DEM [10, 11, 12], and the image-based DEM [13, 14, 15, 16], can be used. For more information on granular materials, the reader can refer to the state-of-the-art review [17].

In MS-DEM, the contact interaction between non-spherical particles is determined based on the interactions between the representing spheres of neighbouring particles. This approach offers high computational efficiency, and reliable contact models such as the Hertz contact model can be employed [18].

In the pure MS-DEM approach, structures are typically modelled using rigid walls, which do not consider structural deformation. To accurately capture the contact interaction between MS-DEM and the structure, it becomes necessary to account for structural deformation. Therefore, the Finite Element Method (FEM) is utilised for analysing structural deformation. Recently, the MS-DEM/FEM coupling method [19] is developed to handle the interaction between granular materials and structures.

In the traditional FEM, the surface of the structure often has a lower geometric approximation for curved surfaces and exhibits lower smoothness at the edges and nodes. This lack of smoothness results in different contact situations between discrete elements (DEs) and finite elements (FEs), such as sphere-node, sphere-edge, and sphere-surface contacts [20, 21], which increases the complexity of the contact detection algorithm. Additionally,

Journal Pre-proof

Journal Pre-proof

when a sphere is located near a node, the contact situation may change [22] in the adjacent time step, for example, from sphere-node to sphere-edge or sphere-surface contact. This change may lead to a significant variation in the contact force/direction in the adjacent time step, giving rise to the time continuity problem. Moreover, the lower geometric approximation of the structure not only reduces the accuracy of the structural analysis but also affects the calculation of the interaction between granular particles and structures.

Isogeometric analysis (IGA), originally proposed by Hughes et al. [23], uses the same basis functions as those describing geometries in CAD [24], e.g. B-spline or NURBS basis functions, to approximate the solution field. Therefore, the geometry of IGA models can be identical to the corresponding CAD models. So the error from geometric approximation is minimised. The IGA model usually has the exact and smooth geometry and the numerical results can generally achieve a high accuracy with relatively smaller number of elements. Because of this advantage, the IGA has been coupled with other method, such as an IGA-BEM (boundary element method) coupling approach [25], the IGA-meshfree coupling approach [26], and a scaled boundary FEM-IGA coupling method [27].

The main aim of the current work is by employing the above advantages offered by IGA and MS-DEM to develop a multi-sphere DEM/IGA coupling method to handle the contact interaction between structures and particles with different shapes. The particles of different shapes are represented and

Journal Pre-proof

Journal Pre-proof

analysed by the MS-DEM while the structures are modeled using IGA. The coupling method is employed to handle the contact interaction between particles and structures. The smoothness of the IGA surface makes the overlap vector between a particle and the IGA surface change continuously during the particle motion, thus avoiding the time continuity problem of the contact force between the particle and the structure in this coupling method. In the global contact search, the CGRID method [28, 29] accompanied by axis aligned bounding boxes (AABBs) and oriented bounding boxes (OBBs) are utilised for the determination of the candidate contact pairs, i.e. MS-DEM and IGA element, and then the combined simplex and Brent iteration is employed to find the contact position. The contact force between each sphere of the MS-DEM and the surface of IGA element is dealt with by a penalty function method based on Hertz-Mindlin contact model [30, 31], and the friction and damping forces are considered. The contact interaction between a MS-DEM and an IGA element can be determined when the contact force between each of the composed spheres and the IGA element is obtained.

The paper is organised as follows. Section 2 provides a short introduction to NURBS basis functions and isogeometric approximations. In Section 3, the basic formulations of multi-sphere discrete element models for particulate systems is reviewed briefly. The coupling approach including global search, local search, and contact force calculation is presented in Section 4. Three numerical examples are presented in Section 5 to assess the accuracy and applicability of the proposed coupling approach. Finally, the conclusions

Journal Pre-proof

drawn from the study are given in Section 6.

2. Isogeometric method

A brief introduction to the isogeometric method is provided below, which is mainly adopted from [32]. More detailed descriptions can be found, for instance, in [23].

2.1. NURBS basis functions

To construct NURBS basis functions, the knot vector $\boldsymbol{k}^I$ for the I^{th} dimension of a 3D patch can be defined as

$$\boldsymbol{k}^I = \left\{ \underbrace{\xi_0^I, \ldots, \xi_{p_I}^I}_{(p_I+1)\text{terms}}, \xi_{p_I+1}^I, \ldots, \xi_i^I, \ldots, \xi_{n_I^{\mathrm{k}}}^I, \underbrace{\xi_{n_I^{\mathrm{k}}+1}^I, \ldots, \xi_{m_I^{\mathrm{k}}}^I}_{(p_I+1)\text{terms}} \right\}, (I = 1, 2, 3) \quad (1)$$

where ξ_i^I denotes the I^{th} knot and is less than or equal to its successor, i.e. $\xi_i^I \le \xi_{i+1}^I$, $i = 0, \ldots, n_I^{\mathrm{k}} + p_I$. p_I is the degree of the B-spline basis functions. The node number, n_I^{e}, of each control mesh in the I^{th} direction is equal to $p_I + 1$, and the total number of all control mesh in the I^{th} direction is $m_I^{\mathrm{k}} = n_I^{\mathrm{k}} + n_I^{\mathrm{e}}$. In the I^{th} dimension, there are $n_I^{\mathrm{k}} + 1$ control nodes.

The B-spline basis function of degree p_I can be determined recursively as

$$\phi_{i,0}(\xi^I) = \begin{cases} 1, & \text{if } \xi_i^I \le \xi^I < \xi_{i+1}^I \\ 0, & \text{otherwise} \end{cases} \quad (2)$$

Journal Pre-proof

and

$$\phi_{i,p_I}(\xi^I) = \frac{\xi^I - \xi_i^I}{\xi_{i+p_I}^I - \xi_i^I}\phi_{i,p_I-1}(\xi^I) + \frac{\xi_{i+p_I+1}^I - \xi^I}{\xi_{i+p_I+1}^I - \xi_{i+1}^I}\phi_{i+1,p_I-1}(\xi^I), \text{ for } p_I \geq 1 \quad (3)$$

For repeated knots, a quotient of the form $\square/0$ may appear in some items on the right side in Eq. (3), and is set to be zero. $\phi_{i,p_I}(\xi^I)$ denotes the i^{th} B-spline basis function with degree p_I, and is referred to as $\phi_i(\xi^I)$ hereafter for conciseness. $\phi_i(\xi^I)$ is equal to zero when $\xi_i^I \notin (\xi_i^I, \xi_{i+p_I+1}^I)$, and is infinitely differentiable if $\xi_i^I \in (\xi_i^I, \xi_{i+1}^I)$. Therefore, within a given knot span (ξ_i^I, ξ_{i+1}^I), at most p_I+1 of the basis shape functions are positive

$$\begin{cases} \phi_m(\xi^I) > 0, \text{ for } m = (i - p_I), \ldots, i \\ \phi_m(\xi^I) = 0, \text{ for } m < (i - p_I) \text{ or } m > i \end{cases} \quad (4)$$

A NURBS surface patch, e.g. $\xi^3 = 1$, can be determined by

$$\mathbf{S}_{ij}(\xi^1, \xi^2) = \sum_{m=m_0}^{i} \sum_{n=n_0}^{j} R_{mn}(\xi^1, \xi^2)\boldsymbol{x}_{mn} \quad (5)$$

where $\boldsymbol{x}_{mn}$ are the position vectors of the control nodes. The shape function $R_{mn}(\xi^1, \xi^2)$ for the control node (m, n), which is the m^{th} and n^{th} node along the ξ^1 and ξ^2 directions, can be defined as:

$$R_{mn}(\xi^1, \xi^2) = \frac{\phi_m(\xi^1)\phi_n(\xi^2)\omega_{mn}}{\sum_{M=m_0}^{i} \sum_{N=n_0}^{j} \phi_M(\xi^1)\phi_N(\xi^2)\omega_{MN}} \quad (6)$$

Journal Pre-proof

Journal Pre-proof

in which ω_{mn} is the weighting factor of the control node (m, n).

To find the closest projection of a point on the NURBS surface, the derivatives of the NURBS surface is necessary (see Section 4.2). The derivatives of the NURBS surface ($\xi^3 = 1$) is given by

$$\frac{\partial \mathbf{S}ij(\xi^1, \xi^2)}{\partial \xi^I} = \sum_{m=m_0}^{i} \sum_{n=n_0}^{j} \frac{\partial R_{mn}(\xi^1, \xi^2)}{\partial \xi^I} \boldsymbol{x}_{mn} \quad (I = 1, 2) \tag{7}$$

with

$$\frac{\partial R_{mn}(\xi^1, \xi^2)}{\partial \xi^I} = \frac{\omega_{mn} \partial [\phi_m(\xi^1)\phi_n(\xi^2)]/\partial \xi^I - R_{mn}(\xi^1, \xi^2)\partial \omega / \partial \xi^I}{\omega} \tag{8}$$

where ω is represented as

$$\omega = \sum_{m=m_0}^{i} \sum_{n=n_0}^{j} \phi_m(\xi^1)\phi_n(\xi^2)\omega_{mn} \tag{9}$$

The derivatives of the other surfaces, e.g. $\xi^i = 0$ (i = 1,2,3), of a NURBS volume can be obtained similarly.

3. Discrete element models

3.1. Equations of motion of multi-sphere discrete elements

The translational and rotational motions of a multi-sphere discrete element are governed by Newton's second law

$$m \frac{d^2 \boldsymbol{u}}{dt^2} = \sum \boldsymbol{f}_c + m \boldsymbol{g} \tag{10}$$

$$\boldsymbol{I}\frac{d\boldsymbol{w}}{dt} = \sum \boldsymbol{T}_c \tag{11}$$

where m and $\boldsymbol{I}$ denote the mass and inertia tensor of the multi-sphere DE; $\boldsymbol{u}$ and $\boldsymbol{w}$ are the translational displacement and the rotational velocity, and $\boldsymbol{f}_c$ and $\boldsymbol{T}_c$ are the contact force and torque acting on the discrete element; $\boldsymbol{g}$ denotes the acceleration due to gravity.

To obtain the rotational motion of the multi-sphere DE, the body-fixed coordinate system is chosen to make sure that the inertia tensor $\boldsymbol{I}$ is a diagonal matrix. This coordinate system is also termed as the principal body frame. In this frame, Eq. (11) can be written as

$$\begin{cases} \dot{w}_x = \left[\sum T_{cx} + w_y w_z (I_y - I_z)\right] / I_x \\ \dot{w}_y = \left[\sum T_{cy} + w_z w_x (I_z - I_x)\right] / I_y \\ \dot{w}_z = \left[\sum T_{cz} + w_x w_y (I_x - I_y)\right] / I_z \end{cases} \tag{12}$$

where I_x, I_y and I_z are the diagonal components of the inertia tensor in the principal body coordinate system; $\dot{\square}$ denotes the first derivative versus time; w_i and T_{ci} $(i = x, y, z)$ denote the components of the rotational velocity and contact torques in the local coordinate system. T_{cx}, T_{cy}, and T_{cz} can be obtained from the corresponding components in the global coordinate system by

$$[T_{cx}, T_{cy}, T_{cz}]^T = \boldsymbol{A} \cdot \boldsymbol{T}_c \tag{13}$$

Journal Pre-proof

Journal Pre-proof

where $\boldsymbol{A}$ is the rotation matrix from the global space to the body-fixed frame, and the superscript T denotes the matrix transpose. Because of the rotational velocities on the right-hand side, Eq. (12) is nonlinear. To accurately integrate the rotational motion, the predictor–corrector algorithm [33] is adopted in this work. For completeness, this algorithm is presented below:

(1) The rotational velocity at the moment t_k is first approximated by

$$w_{fi}^{k} = w_i^{k-\frac{1}{2}} + \dot{w}_i^{k-1}(t^k - t^{k-1})/2, i = x, y, z \tag{14}$$

(2) The rotational acceleration at the time instant t_k is calculated using Eq. (12) as

$$\begin{cases} \dot{w}_x^k = \left[\sum T_{cx} + w_{fy}^k w_{fz}^k (I_y - I_z)\right]/I_x \\ \\ \dot{w}_y^k = \left[\sum T_{cy} + w_{fz}^k w_{fx}^k (I_z - I_x)\right]/I_y \\ \\ \dot{w}_z^k = \left[\sum T_{cz} + w_{fx}^k w_{fy}^k (I_x - I_y)\right]/I_z \end{cases} \tag{15}$$

(3) The rotational velocity at the time instant t_k is predicted by

$$w_i^{k} = w_i^{k-\frac{1}{2}} + \dot{w}_i^{k}(t^k - t^{k-1})/2, i = x, y, z \tag{16}$$

Journal Pre-proof

(4) The rotational acceleration is updated by

$$\begin{cases} \dot{w}_x^k = \left[\sum T_{cx} + w_y^k w_z^k (I_y - I_z)\right] / I_x \\ \dot{w}_y^k = \left[\sum T_{cy} + w_z^k w_x^k (I_z - I_x)\right] / I_y \\ \dot{w}_z^k = \left[\sum T_{cz} + w_x^k w_y^k (I_x - I_y)\right] / I_z \end{cases} \tag{17}$$

(5) The rotational velocity at the moment $t^{k+1/2}$ can be calculated as

$$w_i^{k+\frac{1}{2}} = w_i^{k-\frac{1}{2}} + \dot{w}_i^k (t^{k+\frac{1}{2}} - t^{k-\frac{1}{2}}),\ (i = x, y, z) \tag{18}$$

Note that steps (3)–(4) can be repeated until the convergent criterion is satisfied. For example, the difference of the Euclidean norm for rotational acceleration $[\dot{w}_x^k,\ \dot{w}_y^k,\ \dot{w}_z^k]$ between the two successive iterations reaches a desired tolerance.

The orientation of the body-fixed coordinate system is represented and updated using the singularity free quaternion algorithm [33]. The quaternion is defined as

$$\boldsymbol{q} = [q_1, q_2, q_3, q_4] \tag{19}$$

with

$$q_1^2 + q_2^2 + q_3^2 + q_4^2 = 1 \tag{20}$$

The rotation matrix from the global space to the body-fixed frame can be written as

$$\boldsymbol{A} = \begin{bmatrix} 1-2(q_1^2+q_3^2) & -2(q_1q_2-q_3q_4) & 2(q_2q_3+q_1q_4) \\ -2(q_1q_2+q_3q_4) & 1-2(q_2^2+q_3^2) & -2(q_1q_3-q_2q_4) \\ 2(q_2q_3-q_1q_4) & -2(q_1q_3+q_2q_4) & 1-2(q_1^2+q_2^2) \end{bmatrix} \tag{21}$$

The inverse matrix of $\boldsymbol{A}$, i.e. $\boldsymbol{A}^{-1}$, is given by

$$\boldsymbol{A}^{-1} = \boldsymbol{A}^T \tag{22}$$

Thus when the quaternion is known, the rotation matrices $\boldsymbol{A}$ and $\boldsymbol{A}^{-1}$ can be determined. If the rotation matrix $\boldsymbol{A}$ of the multi-sphere is known at the initial state, the initial value of the quaternion q can be calculated [34, 35].

The quaternion at the moment t_{k+1} can be updated by

$$\boldsymbol{q}^{k+1} = \kappa \boldsymbol{R}^T \boldsymbol{P} \tag{23}$$

with the re-normalisation

$$\kappa = (1+\beta_x^2+\beta_y^2+\beta_z^2)/\det\boldsymbol{R} \tag{24}$$

where $\det\boldsymbol{R}$ denotes the determinant of matrix $\boldsymbol{R}$, and $\boldsymbol{R}$ and $\boldsymbol{P}$ are written

Journal Pre-proof

as

$$\boldsymbol{R} = \begin{bmatrix} 1 & -\beta_z & \beta_x & \beta_y \\ \beta_z & 1 & \beta_y & -\beta_x \\ -\beta_x & -\beta_y & 1 & -\beta_z \\ -\beta_y & \beta_x & \beta_z & 1 \end{bmatrix} \tag{25}$$

and

$$\boldsymbol{P} = \boldsymbol{R}^T \cdot \boldsymbol{q}^k = \begin{bmatrix} q_1^k + \beta_z q_2^k - \beta_x q_3^k - \beta_y q_4^k \\ -\beta_z q_1^k + q_2^k - \beta_y q_3^k + \beta_x q_4^k \\ \beta_x q_1^k + \beta_y q_2^k + q_3^k + \beta_z q_4^k \\ \beta_y q_1^k - \beta_x q_2^k - \beta_z q_3^k + q_4^k \end{bmatrix} \tag{26}$$

with

$$\beta_i = \frac{1}{4} w_i (t^{k+1} - t^k), (i = x, y, z) \tag{27}$$

3.2. Contact model

A multi-sphere DE consists of a number of rigid spheres. Hence, the interaction between multi-sphere DEs can be handled using the Hertz-Mindlin contact model between spheres. The normal contact force can be determined by

$$\boldsymbol{f}_n = \frac{2}{3} S_n \boldsymbol{\delta}_n \tag{28}$$

in which $\boldsymbol{\delta}_n$ is the overlap vector between the contacting spheres, as shown in Fig. 1, and the normal stiffness S_n is defined as

$$S_n = 2E^* \sqrt{r^* \|\boldsymbol{\delta}_n\|}, \tag{29}$$

Journal Pre-proof

where the equivalent radius r^* and Young's modulus E^* are written as

$$r^* = \frac{r_i r_j}{r_i + r_j}, \tag{30}$$

and

$$E^* = \frac{E_i E_j}{(1-\nu_i^2)E_j + (1-\nu_j^2)E_i} \tag{31}$$

in which E_i and E_j are the Young's moduli of the contacting spheres, r_i and r_i denote their radii, and ν_i and ν_j are their Poisson's ratios. The normal

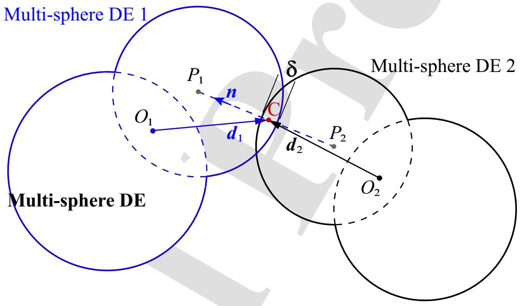

Figure 1: The schematic diagram of two contact MS-DEM

damping force $\boldsymbol{f}_{dn}$ is calculated by

$$\boldsymbol{f}_{dn} = -2\sqrt{\frac{5}{6}}\eta\sqrt{S_n m^*}\boldsymbol{v}'_n \tag{32}$$

where the normal component of the relative velocity between the contacting spheres $\boldsymbol{v}'_n$ is calculated by

$$\boldsymbol{v}'_n = [(\boldsymbol{v}'_{c1} - \boldsymbol{v}'_{c2}) \cdot \boldsymbol{n}]\,\boldsymbol{n} \tag{33}$$

Journal Pre-proof

with

$$\boldsymbol{v}'_{ci} = \boldsymbol{v}'_{pi} + \boldsymbol{w} \times \boldsymbol{d}_i \ (i = 1, 2) \tag{34}$$

and

$$\boldsymbol{n} = (\boldsymbol{p}_1 - \boldsymbol{p}_2) / |\boldsymbol{p}_1 - \boldsymbol{p}_2| \tag{35}$$

where $\boldsymbol{v}'_{ci}$ $(i = 1, 2)$ denotes the velocity of multi-sphere DE i at the contact point C, $\boldsymbol{p}_i$ is the position vector of the sphere centre P_i, $\boldsymbol{n}$ denotes the unit normal direction, $\boldsymbol{d}_i$ denotes the vector from the mass centre of multi-sphere DE i to C, as shown in Fig. 1. The position vector of the contact point C, $\boldsymbol{p}_c$, is determined as

$$\boldsymbol{p}_c = \boldsymbol{p}_1 - (r_1 - 0.5\,|\boldsymbol{\delta}_n|)\boldsymbol{n}, \tag{36}$$

The equivalent mass m^*, and the parameter η are determined by

$$m^* = \frac{m_I m_J}{m_I + m_J}, \tag{37}$$

$$\eta = \frac{\ln\lambda}{\ln^2\lambda + \pi^2} \tag{38}$$

where λ is the coefficient of restitution, and m_I and m_J are the mass of the two multi-sphere DEs. The tangential contact force $\boldsymbol{f}_t$ between the contacting spheres can be determined from the tangential stiffness S_t and the relative tangential displacement $\boldsymbol{\delta}_t$ as

$$\boldsymbol{f}_t = -S_t\boldsymbol{\delta}_t \tag{39}$$

Journal Pre-proof

Journal Pre-proof

with

$$S_t = 8G^* \sqrt{r^* \|\boldsymbol{\delta}_n\|}, \tag{40}$$

and

$$\boldsymbol{\delta}_t = \int_{t_1}^{t_2} \boldsymbol{v}'_t \mathrm{d}t = \int_{t_1}^{t_2} (\boldsymbol{v}' - \boldsymbol{v}'_n) \mathrm{d}t \tag{41}$$

where $\boldsymbol{v}'$ and $\boldsymbol{v}'_n$ are the relative velocity and its normal component at the contact point, and $[t_1, t_2]$ is the time interval of the contact interaction. Here G^* is the equivalent shear modulus, which is defined by

$$G^* = \frac{G_i G_j}{(2-\nu_i)G_j + (2-\nu_j)G_i}, \tag{42}$$

where G_i and G_j are the shear moduli of the contact spheres. In addition, the tangential contact force $\boldsymbol{f}_t$ is limited by the friction force. Therefore, Eq. (39) can be written as

$$\boldsymbol{f}_t = -\min(S_t \|\boldsymbol{\delta}_t\|, f_r) \cdot \frac{\boldsymbol{\delta}_t}{\|\boldsymbol{\delta}_t\|} \tag{43}$$

Here $f_r = \|\boldsymbol{f}_n\|\mu$ is the Coulomb friction, and μ is the coefficient of the friction. The tangential damping force $\boldsymbol{f}_{dt}$ is calculated by

$$\boldsymbol{f}_{dt} = -2\sqrt{\frac{5}{6}}\eta\sqrt{S_t m^*}\boldsymbol{v}'_t \tag{44}$$

Journal Pre-proof

Journal Pre-proof

Then, the resultant force at the contact zone can be obtained

$$\boldsymbol{f}_{rt} = \boldsymbol{f}_n + \boldsymbol{f}_{dn} + \boldsymbol{f}_t + \boldsymbol{f}_{dt} \tag{45}$$

The moment of the resultant force is written as

$$\boldsymbol{T}_c = \boldsymbol{r}_{dc} \times \boldsymbol{f}_{rt} \tag{46}$$

where $\boldsymbol{r}_{dc}$ is the relative position vector from the mass centre to the contact point.

4. Coupling approach

4.1. Global search

The purpose of the global search is to detect the potential contact pairs between NURBS surfaces and multi-sphere DEs. According to the strong convex hull property [32, 36], a NURBS surface or curve is fully enclosed in the convex hull of its control mesh, as shown in Fig. 2 where NURBS curve C_3 is completely contained in convex hull $N_3N_4N_5$. Therefore, the convex hull of a NURBS is used for the global search.

The axis aligned bounding boxes (AABB) of the convex hull and a multi-

Journal Pre-proof

sphere DE are shown in Fig. 2, and can be determined by

$$\begin{cases} \alpha_{\min} = \min(\alpha_1 - r_1, ..., \alpha_i - r_i, ..., \alpha_n - r_n) \\ \\ \alpha_{\max} = \max(\alpha_1 + r_1, ..., \alpha_i + r_i, ..., \alpha_n + r_n) \end{cases}, \ (\alpha = x, y, z) \tag{47}$$

where n denotes the number of spheres (or control nodes) forming the external surface of the multi-sphere DE (or the surface of IGA element), subscript i means that the variable is related to sphere (or node) i, r is sphere radius (or zero for control nodes), and x, y and z denote the coordinates of sphere centre (or control nodes). When all spheres have the same radius, r_0, Eq. (47) can be simplified as

$$\begin{cases} \alpha_{\min} = \min(\alpha_1, ..., \alpha_i, ..., \alpha_n) - r_0 \\ \\ \alpha_{\max} = \max(\alpha_1, ..., \alpha_i, ..., \alpha_n) + r_0 \end{cases}, \ (\alpha = x, y, z) \tag{48}$$

As a convex hull shares the same control nodes as its control mesh, we do not distinguish between a convex hull and its control mesh in the global search. The CGRID search method [28], also called D-Cell in [29], is extended to detect overlapping AABBs of the multi-sphere DEs and the convex hulls of NURBS surfaces which form the potential pairs.

To further eliminate impossible contact interactions, the oriented bounding boxes (OBBs) of the convex hulls of the NURBS surfaces in the potential

Journal Pre-proof

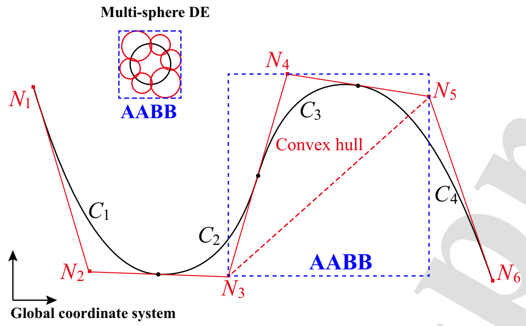

Figure 2: The 2D schematic diagram of the NURBS curve, the multi-sphere, the convex hull, and the AABB boxes

contact pairs are fitted using the $O(n \log n)$-time algorithm [37]. Fig. 3 illustrates the process. The control mesh, represented by triangle $N_3N_4N_5$, consists of three control nodes. The multi-sphere DE is composed of one internal sphere and six external spheres. The external spheres, shown in red, form the external surface of the multi-sphere DE. The OBB $O_cN_3N_5D$ encompasses the control mesh or convex hull, and $\boldsymbol{e}_1$ and $\boldsymbol{e}_2$ are the unit orthogonal vectors of the adjacent edges of the OBB. The vertex O_c of the OBB along with unit vectors $\boldsymbol{e}_1$ and $\boldsymbol{e}_2$, establishes a local coordinate system for the global search.

The coordinates of an external sphere in the local coordinate system are obtained using the following equation:

$$\boldsymbol{x}_i^c = \boldsymbol{T}_o \cdot \boldsymbol{d}_{ri} = \boldsymbol{T}_o \cdot (\boldsymbol{x}_i - \boldsymbol{x}_o), (i = 1, ..., m) \tag{49}$$

where $\boldsymbol{x}_i$ represents the global position vector of sphere i, $\boldsymbol{x}_i^c$ represents the local position vector, $\boldsymbol{d}_{ri}$ is the relative position vector from the origin to sphere i, and m denotes the total number of external spheres in the multi-sphere DE.

The overlapping relationship between sphere i and an OBB can be determined by the following inequalities

$$\begin{cases} \min(x^c_{1\alpha}, ..., x^c_{i\alpha}, ..., x^c_{m\alpha}) < 0 \\ \\ \max(x^c_{1\alpha}, ..., x^c_{i\alpha}, ..., x^c_{m\alpha}) > L_\alpha \end{cases}, \ (\alpha = x, y, z) \tag{50}$$

where $x^c_{i\alpha}$ represents the components of the local position vector $\boldsymbol{x}^c_i$. If any of the inequalities in Eq. (50) is satisfied, it indicates that the sphere overlaps with the OBB. Consequently, the identities (IDs) of the multi-sphere DE and the external spheres are stored for potential contact with the NURBS surfaces. It is important to note that a multi-sphere DE or an external sphere may be in contact with multiple NURBS surfaces. If the external sphere does not overlap with the OBB, this potential contact pair is excluded.

4.2. Local search

The local search is employed in the next phase to determine the precise contact configuration for a potential contact pair identified during the global search phase. Fig. 4 illustrates the contact scenario between a multi-sphere DE and a NURBS. The multi-sphere DE comprises three external spheres, with D representing the centre of the potential contact sphere identified in

Journal Pre-proof

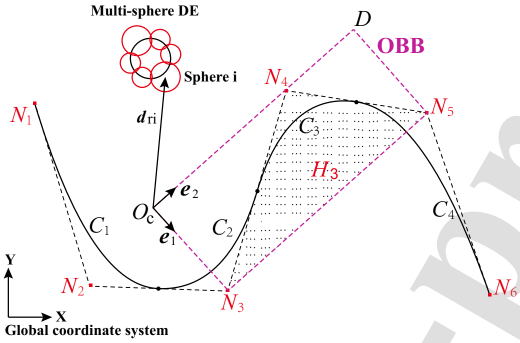

Figure 3: The OBB of the convex hull of the NURBS curve

the global search. C denotes the closest projection of D onto the NURBS, and the closest projection C can be obtained by solving the following two nonlinear equations:

$$\begin{cases} \dfrac{\partial \boldsymbol{x}}{\partial \xi^1}|_{(\xi_c^1,\xi_c^2)}[\boldsymbol{d} - \boldsymbol{x}(\xi_c^1, \xi_c^2)] = 0 \\ \\ \dfrac{\partial \boldsymbol{x}}{\partial \xi^2}|_{(\xi_c^1,\xi_c^2)}[\boldsymbol{d} - \boldsymbol{x}(\xi_c^1, \xi_c^2)] = 0 \end{cases} \tag{51}$$

where $\boldsymbol{x}(\xi_c^1, \xi_c^2)$ represents the position vector of the closest projection C, which we will denote as $\boldsymbol{x}_c$ henceforth; ξ_c^1 and ξ_c^2 are the parameter coordinates of the closest projection C that need to be determined; and $\boldsymbol{d}$ corresponds to the position vector of the sphere centre, D.

The nonlinear equations (51) are solved numerically. In this work, the simplex method, a robust unconstrained optimisation method, is adopted for a preliminary estimation of the parameter coordinates (ξ_c^1, ξ_c^2) of the projec-

Journal Pre-proof

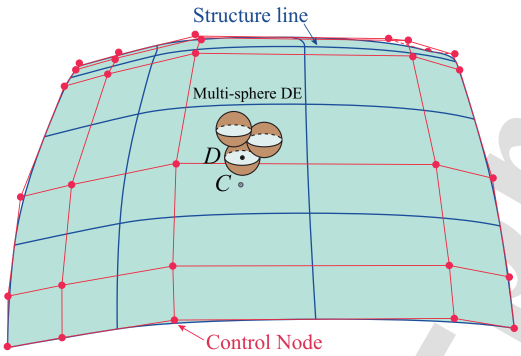

Figure 4: The contact situation of a multi-sphere DE and a NURBS

tion D. Using this estimation as an initial value, more accurate parameter coordinates can be calculated by the Brent iteration [32]. After the position vector of projection D, $\boldsymbol{x}_c$, is obtained, the normal overlap δ_{cn} between the sphere and the NURBS can be calculated by

$$\delta_{cn} = r - \|\boldsymbol{d} - \boldsymbol{x}_c\| \tag{52}$$

If $\delta_{cn} > 0$, the sphere is in contact with the NURBS. Then, the overlap vector can be determined by

$$\boldsymbol{\delta}_{cn} = \delta_{cn}\boldsymbol{n}_c \tag{53}$$

with

$$\boldsymbol{n}_c = \frac{\boldsymbol{d} - \boldsymbol{x}_c}{\|\boldsymbol{d} - \boldsymbol{x}_c\|} \tag{54}$$

Journal Pre-proof

Journal Pre-proof

The tangential overlap vector $\boldsymbol{\delta}_{ft}$ can be calculated as

$$\boldsymbol{\delta}_{ct} = \int_{t_1}^{t_2} \boldsymbol{v}'_{ct} \mathrm{d}t \tag{55}$$

where $[t_1, t_2]$ is the time interval of the contact interaction between the sphere and the NURBS; $\boldsymbol{v}'_{ct}$ is the tangential relative velocity at the contact point on the NURBS, and can be calculated from the relative velocity $\boldsymbol{v}'_c$ and normal component $\boldsymbol{v}'_{cn}$

$$\boldsymbol{v}'_{ct} = \boldsymbol{v}'_c - \boldsymbol{v}'_{cn} \tag{56}$$

with

$$\boldsymbol{v}'_c = \boldsymbol{v}_{dc} - \boldsymbol{v}_{gc} = \boldsymbol{v}_{dc} - \sum_{m=m_0}^{i} \sum_{n=n_0}^{j} R_{mn}(\xi_c^1, \xi_c^2) \boldsymbol{v}_{mn} \tag{57}$$

and

$$\boldsymbol{v}'_{cn} = (\boldsymbol{v}'_c \cdot \boldsymbol{n}_c) \boldsymbol{n}_c \tag{58}$$

where $\boldsymbol{v}_{dc}$ and $\boldsymbol{v}_{gc}$ are the velocities at the contact points on the sphere and the NURBS respectively, and $\boldsymbol{v}_{mn}$ are the node velocities of the control mesh.

4.3. Contact force

After the normal and tangential overlap vectors have been obtained in the local search stage, the contact force between the multi-sphere DE and the IGA element can be calculated. A penalty function method based on the Hertz model [30] is used to determine the contact force as

$$\boldsymbol{f}_{cn} = \frac{2}{3} \gamma S_{cn} \boldsymbol{\delta}_{cn} \tag{59}$$

Journal Pre-proof

Journal Pre-proof

where S_{cn} is the normal stiffness between the DE and IGA element and has the same formula as Eq. (29), and E^* is determined accordingly from the material properties of the contacting particle and the structure. Because the curvature radius of the NURUS in contact is generally much larger than the radius of the sphere, r^* can be set to the sphere radius, and γ is the penalty factor whose default value is 1.0, as established in [36].

The normal damping force $\boldsymbol{f}_{cdn}$ between the DE and the IGA element is given by

$$\boldsymbol{f}_{cdn} = -2\sqrt{\frac{5}{6}}\eta\sqrt{S_{cn}m}\boldsymbol{v}'_{cn} \tag{60}$$

in which m denotes the mass of the multi-sphere DE. The tangential contact force $\boldsymbol{f}_{ct}$ between the sphere and the NURBS is calculated by Eqs. (39) and (43) using the parameters of the contacting DE and IGA element.

The tangential damping force $\boldsymbol{f}_{cdt}$ is computed by

$$\boldsymbol{f}_{cdt} = -2\sqrt{\frac{5}{6}}\eta\sqrt{S_{ct}m}\boldsymbol{v}'_{t} \tag{61}$$

The resultant contact force at the contact point can be determined as

$$\boldsymbol{f}_{rct} = \boldsymbol{f}_{cn} + \boldsymbol{f}_{cdn} + \boldsymbol{f}_{ct} + \boldsymbol{f}_{cdt} \tag{62}$$

The moment induced by $\boldsymbol{f}_{rct}$ and calculated based on Eq. (46) is imposed on the mass centre of the multi-sphere DE. The contact force is distributed to the control nodes of the IGA element by

$$\boldsymbol{f}_{mn} = -R_{mn}(\xi_c^1, \xi_c^2)\boldsymbol{f}_{rct} \tag{63}$$

where $\boldsymbol{f}_{mn}$ is the distributed force for the control node at the m^{th} and n^{th} position.

5. Numerical examples

5.1. One particle impacting a quarter of a cylinder

To evaluate the proposed coupling method, we first conduct a test using an ellipsoical particle impacting a quarter of a hollow cylinder. The geometry of the hollow cylinder, along with its fixed boundary, is depicted in Fig. 5. Initially, the particle makes contact with the centre of the external surface of the hollow cylinder, with its major axis aligned along the symmetrical plane. The impact angle between the major axis and the normal direction at the centre of the external surface is denoted as θ. The particle's initial velocity is 1.0 m/s in the direction normal to the surface. It has a mass of 1.0 g, and its diagonal components of the inertia tensor in the principal body coordinate system are $I_x = 0.784$ g/mm^2, $I_y = 2.842$ g/mm^2, and $I_z = 2.842$ g/mm^2. The material properties of both the particle and the cylinder can be found in Table 1. Furthermore, the restitution coefficient between the particle and the cylinder is set to be 1.0, denoted as λ_c, and no friction is considered.

The ellipsoidal particle is represented by an multi-sphere DE, consisting of

Journal Pre-proof

Journal Pre-proof

Table 1: The material properties of the particle and the cylinder

Young's modulus of particle	E_p	1.0 GPa
Poisson's ratio of particle	ν_p	0.25
Mass density of cylinder	ρ_t	2500 kg/m^3
Young's modulus of cylinder	E_t	1.0 GPa
Poisson's ratio of cylinder	ν_t	0.25

nine spheres with specific sizes and relative positions [38] as depicted in Fig. 6. The hollow cylinder is simulated using 256 quadratic IGA elements with full volume integration. The interaction between the particle and the cylinder is handled using the proposed coupling method. In this method, a penalty factor of 1.0 is utilised, as previous investigations [36] have demonstrated that the Hertz contact model without the penalty factor correction (i.e. using the penalty factor 1.0) achieves optimal performance for the normal contact interaction between a rigid discrete element and a structural element with linear elasticity.

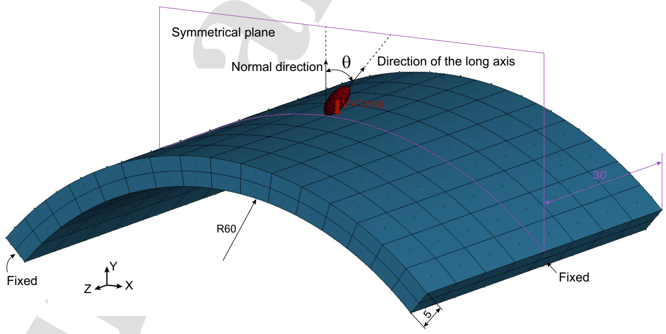

Figure 5: The geometry, loading, and boundary conditions of the particle-cylinder impact system

Journal Pre-proof

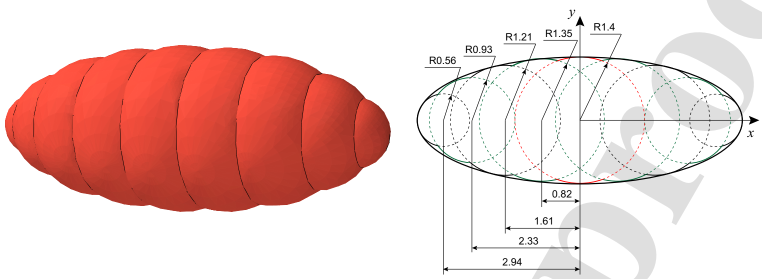

(a) 3D view (b) 2D front view

Figure 6: The geometry of the MS-DEM in the local coordinate system

Three impact angles, namely $\theta = 0°$, $10°$, and $20°$, are simulated using the IGA/MS-DEM coupling method. To validate the accuracy of this coupling method, the same impact cases are also simulated using the finite element method where the multi-sphere DE is represented by an analytical rigid body and the cylinder is modelled using 8-node linear solid elements (C3D8) in Abaqus [39]. The interaction between the particle and the cylinder is handled using a penalty-based constraint enforcement method with a linear pressure-overclosure relationship. As the contact models and overlap definition in FEM differ from those in the coupling method, the contact stiffness in the FEM model may be different from that in the coupling method. The penalty stiffness in the FEM model is determined by ensuring that overlapping region from the FEM simulation is the same as that from the coupling method. Using this technique, the penalty in the FEM model is set to be 2 GPa with a scale factor of 1.0. The surface-to-surface contact algorithm in Abaqus is employed to detect contact between the analytical rigid body and the cylinder.

The results obtained using the proposed coupling method are compared with those obtained using FEM, as depicted in Figs. 7–9. The time histories of the contact force (Fig. 7), particle linear velocity in the Y direction (Fig. 8), and particle angular acceleration in the Z direction (Fig. 9) calculated using the proposed coupling method exhibit good agreement with the results obtained from the FEM. Furthermore, it is observed that a smaller impact angle, θ, generally leads to a higher impact force, a larger rebound velocity, and a smaller angular acceleration.

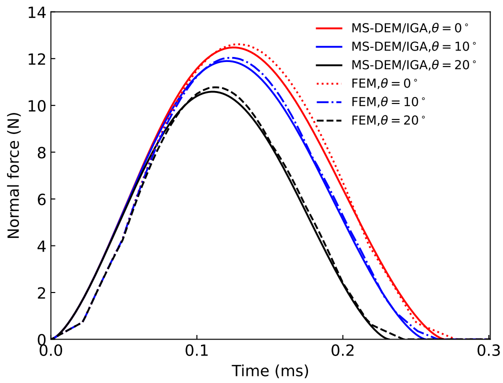

Figure 7: The comparison of the impact force histories for $\theta = 0°$, $10°$, and $20°$ obtained from the proposed coupling method and the FEM

Figure 10 presents a comparison of the displacements in the Y direction at the centre of the free cylindrical surface. Initially, the results obtained using the coupling method exhibit good agreement with those from the FEM. After 0.5 ms, the difference between the FEM and coupling results increases

Journal Pre-proof

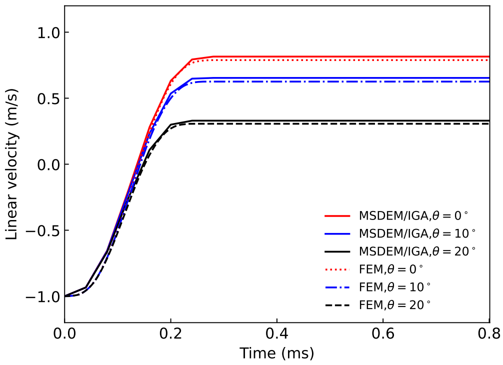

Figure 8: The comparison of the linear velocity histories of the particle in the Y direction for $\theta = 0°$, $10°$, and $20°$ obtained from the proposed coupling method and the FEM

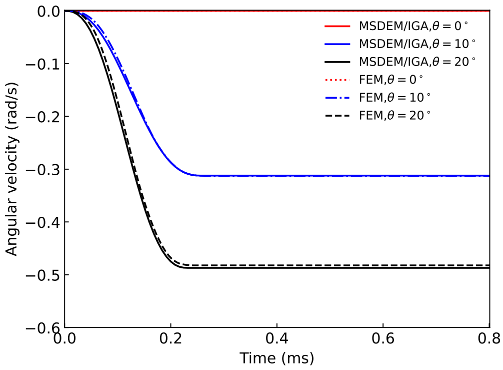

Figure 9: The comparison of the angular velocity histories of of the particle in the Z direction for $\theta = 0°$, $10°$, and $20°$ obtained from the proposed coupling method and the FEM

Journal Pre-proof

slightly, but it remains within an acceptable range. Furthermore, both the FEM and the coupling results show the same trend that a smaller impact angle θ leads to higher displacement peaks in the impact direction.

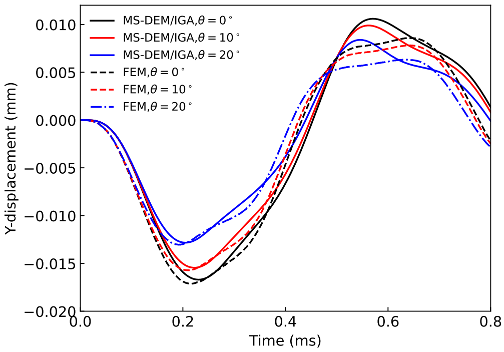

Figure 10: The comparison of the displacement histories in the Y direction for $\theta = 0°$, $10°$, and $20°$ obtained from the proposed coupling method and the FEM

Additionally, three cases with different friction coefficients between the particle and the cylinder, namely $\mu = 0.2$, 0.4, and 0.6, are considered, but the same impact angle $\theta = 20°$ is used. In the FEM model, a penalty friction formulation is employed to calculate the friction force, while the normal behaviour settings remain the same as these in the previous FEM cases. The time histories of the tangential contact force are shown in Fig. 11. The curves obtained using the proposed coupling model are consistent with those obtained using the FEM. Each curve of the cases simulated by the proposed coupling model exhibits a non-smooth point, and the tangential contact force before this point is calculated using the formula similar to Eq. (39). After this point, the tangential contact force is determined by the

Journal Pre-proof

Journal Pre-proof

friction due to the occurrence of slip.

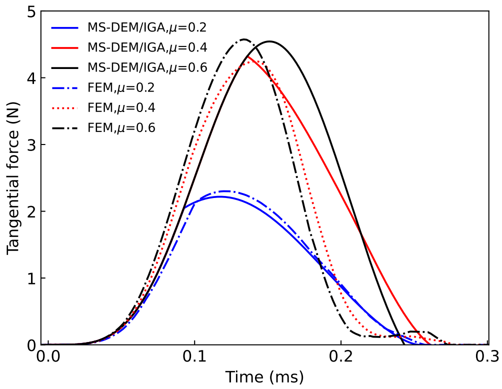

Figure 11: The comparison of the tangential force histories with different friction coefficients, i.e. $\mu = 0.2$, 0.4, and 0.6

5.2. Particles impacting corrugated plate

To further verify the applicability of the IGA/MSDEM coupling approach proposed, the impacting process of granules on a corrugated plate is considered numerically. The geometry of the corrugated plate with a thickness of 5 mm is shown in Fig. 12 where a small region of the corrugated plate is cut off to show the cross section of the protrusion. The four sides of the corrugated plate are fully fixed. Initially, 712 particles located in a cylindrical region move toward the corrugated plate with an initial velocity of 5.0 m/s. The size of the particles is identical. At the initial state, the particles in the bottom layer are just in contact with the wave crest of the top surface of the corrugated plate. The material constants of the particles and the corrugated plate are the same as those listed in Table 1.

Journal Pre-proof

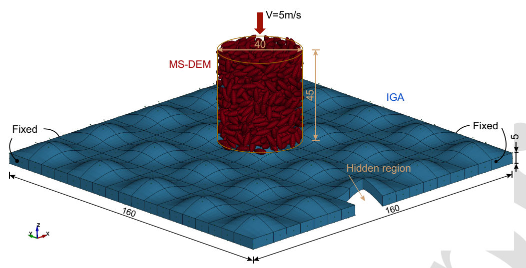

Figure 12: The geometry, boundary conditions and loading of the particle impacting system in which a region of the corrugated plate is cut off for the visibility of the cross section of the protrusion

Each ellipsoidal particle is modelled using the same multi-sphere DE as illustrated in Fig. 6 in Section 5.1. Each particle has a mass of 0.1 g, and its principal moments of inertia along the x, y, and z axes in the body frame are 0.0784 g/mm^2, 0.2842 g/mm^2, and 0.2842 g/mm^2, respectively. Initially, the orientations and positions of the multi-sphere DEs are randomly distributed within the cylindrical region, and the multi-sphere DEs are not in contact with each other.

The corrugated plate is modelled using 324 second-degree solid elements of IGA. The material properties of the particles and the corrugated plate are the same as those of the particle and the cylinder in in Section 5.1, respectively. The contact interaction between the multi-sphere DEs and the IGA elements is handled by the proposed coupling approach with a penalty factor of 1.0. The restitution coefficient between the particles and the corrugated plate is 0.4, while the friction coefficient between them is 0.5. The time step used in the central difference method is 5.0×10^{-5} ms.

The impact force history acting on the corrugated plate is plotted together with the displacement history at the centre of the free surface of the corrugated plate, as shown in Fig. 13. In the time interval [1, 4] ms, the impact force reaches relatively high values, and the centre of the free surface experiences large displacements. After 6 ms, both the impact force and the displacement remain relatively small.

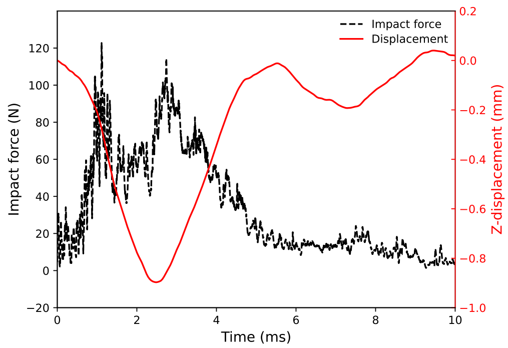

Figure 13: The time histories of the impact force and the displacement along the vertical direction at the centre of the free surface

The impact process and velocity distributions of the particle-plate system are depicted in Figure 14. Initially, some particles make contact with the wave crest of the corrugated plate (Figure 14(a)). Around 1.2 ms, a group of particles collide with the plate's valley (Figure 14(b)). Due to the contact interaction with the plate, the velocities of particles at the bottom decrease significantly, becoming much smaller than those of particles on the top (see Figure 14(c)). As the impact progresses, the particles spread to surrounding areas, resulting in an increased contact area. The number of particles with

Journal Pre-proof

high velocities along the impact direction decreases notably, as shown in Figures 14(d) and 14(e). The configurations and velocity distributions at 8 ms are displayed in Figure 14(f). Throughout the impact process, the particle-plate penetration is minimal, and no excessive penetration occurs.

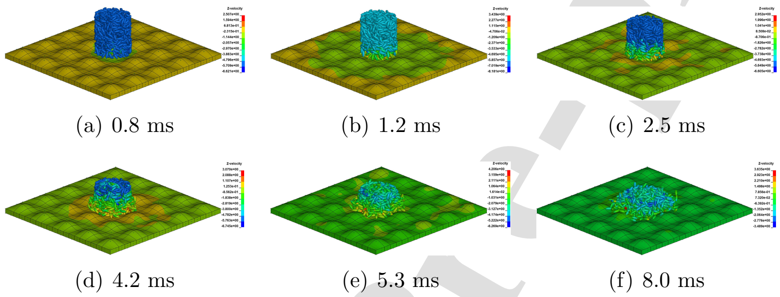

(a) 0.8 ms (b) 1.2 ms (c) 2.5 ms

(d) 4.2 ms (e) 5.3 ms (f) 8.0 ms

Figure 14: The velocity distribution of the multi-sphere particles and the corrugated plate along the vertical direction at different time instants

5.3. Particles of different shapes impacting a chute

To further validate the robustness and applicability of the proposed coupling method, we investigate the impact process of particles with different shapes on a chute in this section. Initially, a total of 8345 particles with random orientations are positioned within a cylindrical region, as depicted in Fig. 15. These particles can be classified into two groups based on their shapes. The first group consists of particles composed of four spheres [40], as illustrated in Fig. 16. The second group comprises particles with the same shape and size as shown in Fig. 6. The number of particles in the first group is 3232, while the second group contains 5113 particles.

Journal Pre-proof

Journal Pre-proof

The particles move towards the chute with an initial velocity of 3 m/s along the z direction. The chute's geometry and boundary conditions are depicted in Fig. 15, where the flat surfaces on the sides of the chute have a parallelogram shape and are fully fixed. In this impact system, gravity is considered with an acceleration of 9.8 m/s^2.

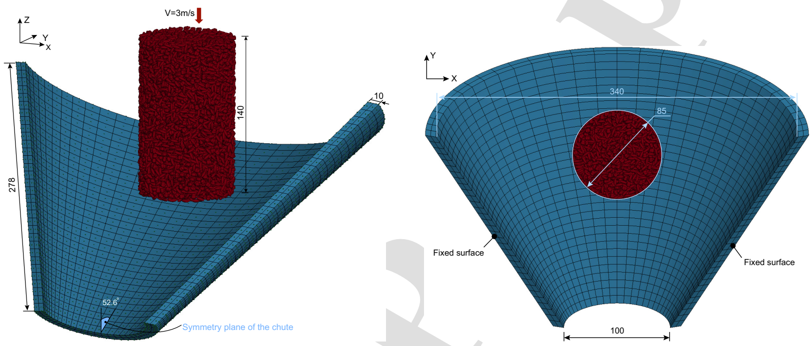

(a) Oblique view (b) Top view

Figure 15: The geometry, loading and boundaries of the particle-chute impact system

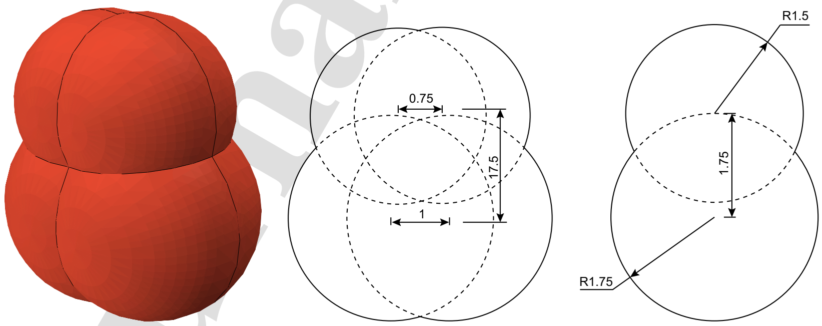

(a) 3D view (b) 2D front view (c) 2D left view

Figure 16: The geometry of the multi-sphere particle

Journal Pre-proof

Journal Pre-proof

The first group of particles has a mass of 0.1 g, and its principal components of the inertia tensor are $I_x = 0.2072$ g/mm^2, $I_y = 0.1649$ g/mm^2, and $I_z = 0.2470$ g/mm^2. In the second group, the mass and inertia tensor of the particles are one-tenth of those in Section 5.1, i.e., $m = 0.1$ g, $I_x = 0.0784$ g/mm^2, $I_y = 0.2842$ g/mm^2, and $I_z = 0.2842$ g/mm^2. The material parameters of the particles and the chute are listed in Table 2.

Table 2: The material properties of the particles and the chute

Young's modulus of particles	E_p	1.0 GPa
Poisson's ratio of particles	ν_p	0.2
Mass density of chute	ρ_t	2500 kg/mm^3
Young's modulus of chute	E_t	3.0 GPa
Poisson's ratio of chute	ν_t	0.3

The particles are simulated using the MS-DEM, while the chute with a curved smooth surface is analyzed using IGA with 2048 elements. The contact interaction between the particles and the chute is handled by the proposed coupling method. The restitution and friction coefficients are 0.1 and 0.15, respectively, for the particle-particle and particle-chute contact interactions. The time step is set to be 5×10^{-5} ms.

The time histories of the impact force acting on the chute and the resultant displacement at the projection of the cylinder axis onto the chute's impact surface are shown in Fig. 17. The resultant impact force exhibits a similar trend to the resultant displacement. Generally, both the resultant displacement and impact force increase from 0 ms to 10 ms, then remain relatively high, and but begin to decrease at around 35 ms. Initially, there

449 is no impact force because the particles are not in contact with the chute.

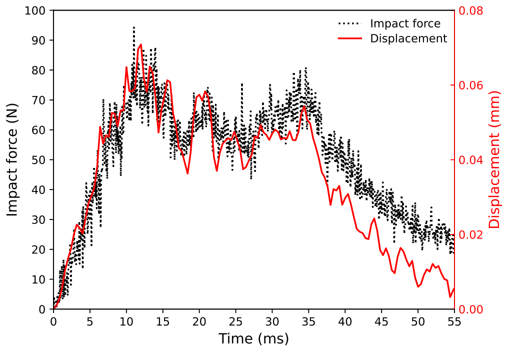

Figure 17: The time histories of the resultant impact force and displacement at the projection of the cylinder axis on the chute impact surface

450 The resultant velocity distributions of the particles and the chute are
451 illustrated in Fig. 18. Initially, the bottom particles on the back side make
452 contact with the curved upper surface of the chute, as depicted in Fig. 18(a).
453 As the particles move downward, the bottom particles in the cylinder region
454 gradually come into contact with the curved upper surface of the chute (refer
455 to Figs. 18(b) and 18(c)). Due to the contact interaction with the chute,
456 the particles scatter and the cylinder region decreases in size, as shown in
457 Fig. 18(d). Over time, the cylinder region nearly disappears, and most of
458 the particles continue to move downward along the curved surface under the
459 influence of gravity, as seen in Fig. 18(e). The contact region between the
460 particles and the chute continues to expand, and some particles even reach
461 the outlet of the chute (see Fig. 18(f)). Throughout this impact process, the
462 particle motions are reasonable, and there are no instances of unreasonable

Journal Pre-proof

penetration between the particles and the chute.

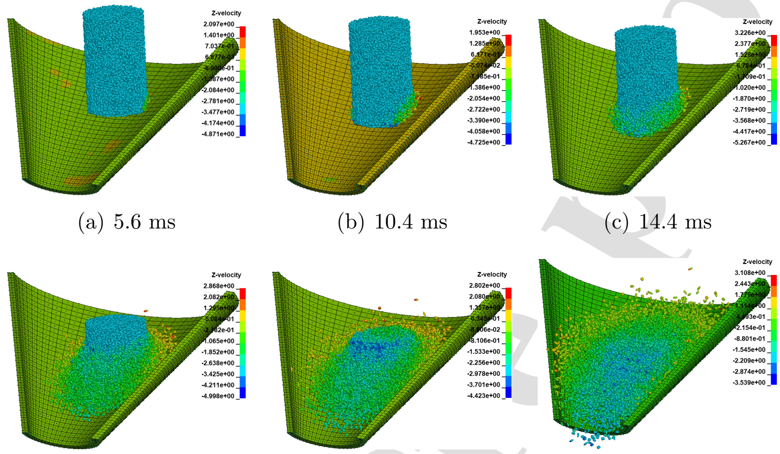

(a) 5.6 ms (b) 10.4 ms (c) 14.4 ms

(d) 30 ms (e) 37.2 ms (f) 50.0 ms

Figure 18: The resultant velocity distribution of the multi-sphere particles and the chute at different time instants

6. Conclusions

A three-dimensional isogeometric/multi-sphere discrete-element coupling method has been presented. This coupling method takes the advantages of the ability of particle shape presentation, high efficiency and excellent robustness of contact searching in multi-sphere discrete element modeling, and the geometry smoothness and accuracy in isogeometric analysis (IGA). In the coupling stage, candidate contact pairs are detected by modifying the CGRID method accompanied by AABB and OBB boxes while the contact position is found by solving the non-linear equations using the simplex and

Journal Pre-proof

Journal Pre-proof

Brent iterations. The contact interaction between IGA and multi-sphere DEM is equivalent to the sphere-IGA contact force handling by a nonlinear penalty function method. Furthermore, a coupled IGA/MS-DEM program has been developed. The accuracy of numerical solutions of the particle impacting a quarter of a cylinder example based on the 3D coupling model has been assessed in the elastic region in comparison with the corresponding FEM model. The applicability and robustness of the coupling approach for modeling the contact interactions between granular particles and structures have also been verified by the two examples, i.e. particles impacting corrugated plate and particles of different shapes impacting a chute.

Acknowledgment

The authors would like to express their gratitude for the financial support provided by the National Natural Science Foundation of China (NOs 51878184 and 12072217) and the research funding from Smart Medical Innovation Technology Center of Guangdong University of Technology (NO. ZYZX22026).

References

[1] Cundall PA. A computer model for simulating processive, large-scale movement in block rock system. In: Proceedings of the International Symposium on Rock Mechanics, 1971. Symp ISRM Proc, Nancy, France; 1971, p. 129–39.

Journal Pre-proof

Journal Pre-proof

[2] Cundall PA, Strack OD. A discrete numerical model for granular assemblies. Geotechnique 1979;29(1):47–65.

[3] Feng Y. An energy-conserving contact theory for discrete element modelling of arbitrarily shaped particles: Basic framework and general contact model. Computer Methods in Applied Mechanics and Engineering 2021;373:113454.

[4] Favier J, Abbaspour-Fard M, Kremmer M, Raji A. Shape representation of axi-symmetrical, non-spherical particles in discrete element simulation using multi-element model particles. Engineering computations 1999;.

[5] Jensen RP, Bosscher PJ, Plesha ME, Edil TB. DEM simulation of granular media—structure interface: effects of surface roughness and particle shape. International journal for numerical and analytical methods in geomechanics 1999;23(6):531–47.

[6] Zhan L, Peng C, Zhang B, Wu W. A surface mesh represented discrete element method (SMR-DEM) for particles of arbitrary shape. Powder Technology 2021;377:760–79.

[7] Peng C, Zhan L, Wu W, Zhang B. A fully resolved SPH-DEM method for heterogeneous suspensions with arbitrary particle shape. Powder Technology 2021;387:509–26.

[8] Feng Y. An effective energy-conserving contact modelling strategy for spherical harmonic particles represented by surface triangular meshes

Journal Pre-proof

Journal Pre-proof

with automatic simplification. Computer Methods in Applied Mechanics and Engineering 2021;379:113750.

[9] Su D, Wang X, Wang X. An in-depth comparative study of three-dimensional angularity indices of general-shape particles based on spherical harmonic reconstruction. Powder Technology 2020;364:1009–24.

[10] Jerves AX, Kawamoto RY, Andrade JE. A geometry-based algorithm for cloning real grains. Granular Matter 2017;19:1–10.

[11] Jerves AX, Kawamoto RY, Andrade JE. Effects of grain morphology on critical state: a computational analysis. Acta Geotechnica 2016;11(3):493–503.

[12] Wang S, Ji S. A unified level set method for simulating mixed granular flows involving multiple non-spherical dem models in complex structures. Computer Methods in Applied Mechanics and Engineering 2022;393:114802.

[13] Zhang X, Tahmasebi P. Drafting, kissing and tumbling process of two particles: The effect of morphology. International Journal of Multiphase Flow 2023;160:104379.

[14] Zhang X, Tahmasebi P. Investigation of particle shape and ambient fluid on sandpiles using a coupled micro-geomechanical model. Powder Technology 2022;409:117711.

Journal Pre-proof

Journal Pre-proof

[15] Zhang X, Tahmasebi P. Coupling irregular particles and fluid: Complex dynamics of granular flows. Computers and Geotechnics 2022;143:104624.

[16] Hosseini MA, Tahmasebi P. On the influence of the natural shape of particles in multiphase fluid systems: Granular collapses. Computers and Geotechnics 2023;162:105654.

[17] Tahmasebi P. A state-of-the-art review of experimental and computational studies of granular materials: Properties, advances, challenges, and future directions. Progress in Materials Science 2023;:101157.

[18] Berry N, Zhang Y, Haeri S. Contact models for the multi-sphere discrete element method. Powder Technology 2023;416:118209.

[19] Guo X, Zheng Z, Zang M, Chen S. A multi-sphere DE-FE method for traveling analysis of an off-road pneumatic tire on irregular gravel terrain. Engineering Analysis with Boundary Elements 2022;139:293–312.

[20] Gao W, Tan Y, Jiang S, Zhang G, Zang M. A virtual-surface contact algorithm for the interaction between FE and spherical DE. Finite Elements in Analysis and Design 2016;108:32–40.

[21] Gao W, Zang M. The simulation of laminated glass beam impact problem by developing fracture model of spherical DEM. Engineering Analysis with Boundary Elements 2014;42:2–7.

Journal Pre-proof

Journal Pre-proof

[22] Zang M, Gao W, Lei Z. A contact algorithm for 3D discrete and finite element contact problems based on penalty function method. Computational Mechanics 2011;48(5):541–50.

[23] Hughes TJ, Cottrell JA, Bazilevs Y. Isogeometric analysis: CAD, finite elements, NURBS, exact geometry and mesh refinement. Computer Methods in Applied Mechanics and Engineering 2005;194(39-41):4135–95.

[24] Cottrell JA, Hughes TJ, Bazilevs Y. Isogeometric analysis: toward integration of CAD and FEA. John Wiley & Sons; 2009.

[25] Chen L, Liu C, Zhao W, Liu L. An isogeometric approach of two dimensional acoustic design sensitivity analysis and topology optimization analysis for absorbing material distribution. Computer Methods in Applied Mechanics and Engineering 2018;336:507–32.

[26] Li W, Nguyen-Thanh N, Zhou K. Geometrically nonlinear analysis of thin-shell structures based on an isogeometric-meshfree coupling approach. Computer Methods in Applied Mechanics and Engineering 2018;336:111–34.

[27] Chasapi M, Klinkel S. A scaled boundary isogeometric formulation for the elasto-plastic analysis of solids in boundary representation. Computer Methods in Applied Mechanics and Engineering 2018;333:475–96.

Journal Pre-proof

Journal Pre-proof

[28] Williams JR, Perkins E, Cook B. A contact algorithm for partitioning n arbitrary sized objects. Engineering Computations 2004;21(2/3/4):235–48.

[29] Han K, Feng Y, Owen D. Sphere packing with a geometric based compression algorithm. Powder Technology 2005;155(1):33–41.

[30] Mindlin RD. Compliance of elastic bodies in contact. Journal of Applied Mechanics 1949;16(3):259–68.

[31] Mindlin RD, Deresiewicz H. Elastic spheres in contact under varying oblique forces. Journal of Applied Mechanics 1953;20(3):327–44.

[32] Gao W, Wang J, Yin S, Feng Y. A coupled 3D isogeometric and discrete element approach for modeling interactions between structures and granular matters. Computer Methods in Applied Mechanics and Engineering 2019;354:441–63.

[33] Walton O, Braun R. Simulation of rotary-drum and repose tests for frictional spheres and rigid sphere clusters. Tech. Rep.; Lawrence Livermore National Lab., CA (United States); 1993.

[34] Sarabandi S, Thomas F. Accurate computation of quaternions from rotation matrices. In: Advances in Robot Kinematics 2018. Springer; 2018, p. 39–46.

[35] Sarabandi S, Thomas F. A survey on the computation of quaternions from rotation matrices. Journal of Mechanisms and Robotics 2019;11(2).

Journal Pre-proof

Journal Pre-proof

[36] Gao W, Feng Y. A coupled 3D discrete elements/isogeometric method for particle/structure interaction problems. Computational Particle Mechanics 2020;7:869–80.

[37] Gottschalk SA. Collision queries using oriented bounding boxes. The University of North Carolina at Chapel Hill; 2000.

[38] Han Y, Zhao D, Jia F, Qiu H, Li A, Bai S. Experimental and numerical investigation on the shape approximation of rice particle by multi-sphere particle models. Advanced Powder Technology 2020;31(4):1574–86.

[39] Systèmes D. Abaqus analysis user's guide. Dassault Systèmes Simulia Corp; Proidence, Rhode Island, USA; 2014. URL: http://130.149.89.49:2080/v6.14/books/usb/default.htm.

[40] Tao H, Jin B, Zhong W, Wang X, Ren B, Zhang Y, et al. Discrete element method modeling of non-spherical granular flow in rectangular hopper. Chemical Engineering and Processing: Process Intensification 2010;49(2):151–8.

Journal Pre-proof

Journal Pre-proof

Highlights (for review)

Highlights

- An isogeometric/multi-sphere discrete-element (MS-DE) coupling method is presented.
- The normal contact force is obtained by a penalty based Hertz-Mindlin contact model.
- The damping and friction forces between MS-DE and IGA are also considered.
- The accuracy and validity of the coupling method are compared with FEM.
- The applicability and robustness of the proposed method is further assessed.

Journal Pre-proof

Journal Pre-proof

Graphical Abstract (for review)

Click here to access/download;Graphical Abstract (for review);Graphical Abstract-5.pdf

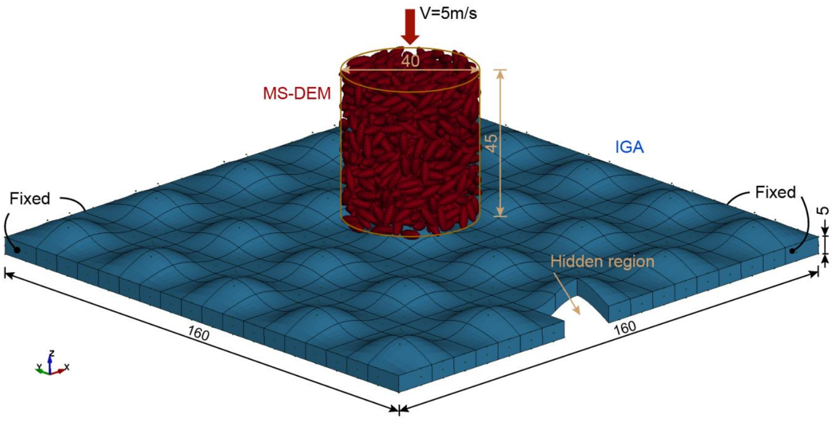

The model of multi-sphere discrete elements impacting an IGA plate

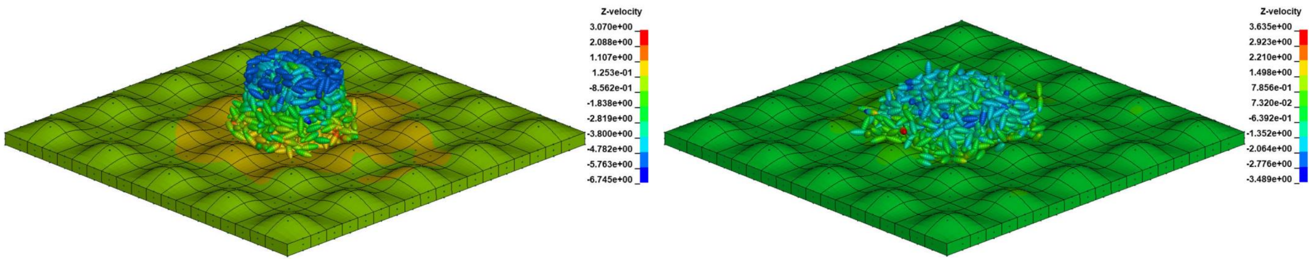

(a) t = 4.2 ms **(a) t = 8.0 ms**

The velocity distribution of the multi-sphere discrete elements and the IGA plate along the vertical direction at (a) 4.2 ms and (b) 8.0 ms

Journal Pre-proof

CRediT authorship contribution statement

Wei Gao: Conceptualization, Methodology, Programming, Validation, Formal analysis, Writing – original draft, Writing – review & editing.

Y.T. Feng: Conceptualization, Methodology, Formal analysis, Writing – review & editing.

Chengyong Wang: Conceptualization, Writing – review & editing.

Journal Pre-proof

Journal Pre-proof

Declaration of Interest Statement

Declaration of interests

☐The authors declare that they have no known competing financial interests or personal relationships that could have appeared to influence the work reported in this paper.

☒The authors declare the following financial interests/personal relationships which may be considered as potential competing interests:

Wei Gao reports financial support was provided by National Natural Science Foundation of China. YT Feng reports financial support was provided by National Natural Science Foundation of China.

Journal Pre-proof